

Single-particle dissipation in TDHF studied from a phase-space perspective

N. Loeb1, A. S. Umar2, J.A. Maruhn1, P.-G. Reinhard3, P.D. Stevenson4, and V. E., Oberacker2

¹*Institut fuer Theoretische Physik, Universitaet Frankfurt, D-60438 Frankfurt, Germany*

²*Department of Physics and Astronomy, Vanderbilt University, Nashville, Tennessee 37235, USA*

³*Institut fuer Theoretische Physik II, Universitaet Erlangen-Nuernberg, D-91058 Erlangen, Germany and*

⁴*Department of Physics, University of Surrey, Guildford, GU2 7XH, UK*

(Dated: August 30, 2012)

We study dissipation and relaxation processes within the time-dependent Hartree-Fock approach using the Wigner distribution function. On the technical side we present a geometrically unrestricted framework which allows us to calculate the full six-dimensional Wigner distribution function. With the removal of geometrical constraints, we are now able to extend our previous phase-space analysis of heavy-ion collisions in the reaction plane to unrestricted mean-field simulations of nuclear matter on a three-dimensional Cartesian lattice. From the physical point of view we provide a quantitative analysis on the stopping power in TDHF. This is linked to the effect of transparency. For the medium-heavy $^{40}\text{Ca}+^{40}\text{Ca}$ system we examine the impact of different parametrizations of the Skyrme force, energy-dependence, and the significance of extra time-odd terms in the Skyrme functional.

PACS numbers: 21.60.-n, 21.60.Jz

I. INTRODUCTION

Time-dependent Hartree-Fock (TDHF) theory provides a fully self-consistent mean-field approach to nuclear dynamics. First employed in the late 1970's [1–4] the applicability of TDHF was constrained by the limited computational power. Therefore, early applications treated the problem in only one spatial dimension, utilizing a very simplified parametrization of the nuclear interaction. Due to the increase in computational power, state-of-the-art TDHF calculations are now feasible in three-dimensional coordinate space, without any symmetry restrictions and using the full Skyrme interaction [5–10].

In this work the Wigner distribution function [11] is calculated as an analysis tool to probe the phase space behavior in TDHF evolution of nuclear dynamics. In comparison to previous work [12], where the Wigner analysis was performed in one and two dimensions, we are now able to carry out both the TDHF simulation and the phase-space analysis in three dimensions. Transformation from coordinate-space representation to phase-space representation, i.e. calculating the Wigner distribution from the density matrix, still remains a computationally challenging problem. Here, we present a fully three-dimensional analysis which allows the study of relaxation processes simultaneously in all directions in k -space. An early one-dimensional study of the Wigner function for TDHF can be found in [13].

The paper is outlined as follows: In Sec. II we introduce the Wigner distribution function and discuss the numerical framework used in this work. We then introduce the principal observables summarizing the local or global momentum-space properties of the Wigner function. First the quadrupole operator in momentum space which gives rise to the usual deformation parameters β and γ to probe relaxation processes in dynamical calcu-

lations. In addition, we define an estimate for the occupied phase-space volume to obtain a relation between the fragment separation in momentum and coordinate space.

Sec. III provides a detailed discussion of the central $^{40}\text{Ca}+^{40}\text{Ca}$ collision, paying particular attention to the effect of transparency. We discuss the impact of different Skyrme parametrizations on the relaxation behavior, as well as the dependence on the center-of-mass energy for a fixed Skyrme interaction. We also examine the influence of extra time-odd terms in the Skyrme functional.

II. OUTLINE OF FORMALISM

A. Solution of the TDHF equations

The TDHF equations are solved on a three-dimensional Cartesian lattice with a typical mesh spacing of 1 fm. The initial setup of a dynamic calculation needs a static Hartree-Fock run, whereby the stationary ground states of the two fragments are computed with the damped-gradient iteration algorithm [14, 15]. The TDHF runs are initialized with energies above the Coulomb barrier at some large but finite separation. The two ions are boosted with velocities obtained by assuming that the two nuclei arrive at this initial separation on a Coulomb trajectory. The time propagation is managed by utilizing a Taylor-series expansion of the time-evolution operator [16] up to sixth order with a time step of $t = 0.2$ fm/c. The spatial derivatives are calculated using the fast Fourier transforms (FFT).

B. Computing the Wigner function

The Wigner distribution function is obtained by a partial Fourier transform of the density matrix $\rho(\mathbf{r}-\frac{\mathbf{s}}{2}, \mathbf{r}+\frac{\mathbf{s}}{2}, t)$,

with respect to the relative coordinate $\mathbf{s} = \mathbf{r} - \mathbf{r}'$

$$f_W^{(3)}(\mathbf{r}, \mathbf{k}, t) = \int \frac{d^3 s}{(2\pi)^3} e^{-i\mathbf{k}\cdot\mathbf{s}} \rho(\mathbf{r} - \frac{\mathbf{s}}{2}, \mathbf{r} + \frac{\mathbf{s}}{2}, t), \quad (1)$$

$$\rho(\mathbf{r}, \mathbf{r}', t) = \sum_l \Psi_l^\dagger(\mathbf{r}, t) \Psi_l(\mathbf{r}', t). \quad (2)$$

Because f_W is not positive definite, it is misleading to consider the Wigner function as a phase-space probability distribution. We will refer to the appearance of negative values for f_W in Sec. III.

Evaluating the Wigner function in six-dimensional phase space is still a computational challenge and only possible employing full Open MP parallelization and extensive use of FFT's. The determining factor is the grid size, which results in

$$N_x^2 \log(N_x) \star N_y^2 \log(N_y) \star N_z^2 \log(N_z) \quad (3)$$

steps to provide the Wigner transform in full space, where N_x, N_y, N_z are the grid points in each direction. Storing the Wigner function reduced to the reaction plane, i.e. $f_W^{(3)}(x, y = 0, z, \mathbf{k})$ at one time step will consume ~ 140 Mb of disk space for the applications presented in Sec. III. Going to larger grid sizes, needed for heavier systems, and/or storing the full three-dimensional Wigner function will clearly result in entering the Gb regime.

C. Observables

In this section we discuss some of the observables used in our analysis. In order to avoid any misunderstandings we will label all observables evaluated in momentum space with a subscript k , and all observables in coordinate space with a subscript r .

1. Quadrupole in momentum space

As an observable to probe relaxation in phase-space quantitatively, we evaluate the quadrupole operator in momentum space. The local deviation of the momentum distribution from a spherical shape is a direct measure for equilibration. The local quadrupole tensor in k -space is given by

$$Q_k^{ij}(\mathbf{r}, t) = \int d^3 k [3\langle k_i(\mathbf{r}, t) \rangle \langle k_j(\mathbf{r}, t) \rangle - \langle \mathbf{k}^2(\mathbf{r}, t) \rangle \delta_{ij}] , \quad (4)$$

using the m -th moment from the local momentum distribution

$$\langle \mathbf{k}^{(m)}(\mathbf{r}, t) \rangle = \frac{\int d^3 k (\mathbf{k} - \langle \mathbf{k}(\mathbf{r}, t) \rangle)^m f_W^{(3)}(\mathbf{r}, \mathbf{k}, t)}{\int d^3 k f_W^{(3)}(\mathbf{r}, \mathbf{k}, t)}, \quad (5)$$

with $\langle \mathbf{k}(\mathbf{r}, t) \rangle$ denoting the average local flow

$$\langle \mathbf{k}(\mathbf{r}, t) \rangle = \frac{\int d^3 k \mathbf{k} f_W^{(3)}(\mathbf{r}, \mathbf{k}, t)}{\int d^3 k f_W^{(3)}(\mathbf{r}, \mathbf{k}, t)}. \quad (6)$$

The spherical quadrupole moments $Q_k^{20}(\mathbf{r}, t)$ and $Q_k^{22}(\mathbf{r}, t)$ are computed by diagonalization of $Q_k^{ij}(\mathbf{r}, t)$

$$Q_k^{20}(\mathbf{r}, t) = \sqrt{\frac{5}{16\pi}} \lambda_3 \quad (7)$$

$$Q_k^{22}(\mathbf{r}, t) = \sqrt{\frac{5}{96\pi}} (\lambda_2 - \lambda_1) \quad (8)$$

with $\lambda_3 > \lambda_2 > \lambda_1$ labeling the eigenvalues of $Q_k^{ij}(\mathbf{r}, t)$. Switching to polar notation the observables

$$\beta_k(\mathbf{r}, t) = \sqrt{\beta_{20}^2(\mathbf{r}, t) + 2\beta_{22}^2(\mathbf{r}, t)} \quad (9)$$

$$\gamma_k(\mathbf{r}, t) = \left| \arctan \frac{\sqrt{2}\beta_{22}(\mathbf{r}, t)}{\beta_{20}(\mathbf{r}, t)} \frac{180^\circ}{\pi} \right|, \quad (10)$$

are obtained via the dimensionless quantities

$$\beta_k^{20}(\mathbf{r}, t) = \frac{4\pi Q_{20}}{5r_k^2 \rho(\mathbf{r}, t)} \quad (11)$$

$$\beta_k^{22}(\mathbf{r}, t) = \frac{4\pi Q_{22}}{5r_k^2 \rho(\mathbf{r}, t)}, \quad (12)$$

where

$$r_k(\mathbf{r}, t) = \sqrt{\langle \mathbf{k}(\mathbf{r}, t) \rangle^2 / \rho(\mathbf{r}, t)}, \quad (13)$$

accounts for the local rms-radius in k -space. The norm is defined such that

$$\rho(\mathbf{r}, t) = \int d^3 k f_W^{(3)}(\mathbf{r}, \mathbf{k}, t). \quad (14)$$

In the presented formalism it is straightforward to define global observables. The global quadrupole tensor is calculated by spatial integration

$$Q_k^{ij}(t) = \int d^3 r \rho(\mathbf{r}, t) Q_k^{ij}(\mathbf{r}, t). \quad (15)$$

Applying the same diagonalization as in the local case (7) we end up with a global definition for $\beta_k^{20}(t)$ and $\beta_k^{22}(t)$. For the following results we exclusively use the global definition since it is more compact and allows the simultaneous visualization of multiple time-dependent observables.

2. Quadrupole in coordinate space

To illustrate the global development of a reaction, we will also use the expectation value $Q_r^{20} \equiv \langle \hat{Q}_r^{20} \rangle$ of the quadrupole operator in coordinate space.

3. Occupied phase space volume

To give a rough measure for the phase-space volume occupied by the fragments during a heavy-ion collision

we assume a spherical shape of the local momentum distribution. Adding up the k -spheres

$$V_k(\mathbf{r}, t) = \frac{4\pi}{3} \langle \mathbf{k}^2(\mathbf{r}, t) \rangle^{3/2}, \quad (16)$$

leads to the total occupied phase-space volume

$$V_k(t) = \int d^3r V_k(\mathbf{r}, t). \quad (17)$$

III. RESULTS AND DISCUSSION

It is the aim of this work to provide a quantitative analysis of the magnitude of relaxation processes occurring in TDHF. Therefore we will vary a single reaction parameter, while all the other parameters are fixed. The $^{40}\text{Ca}+^{40}\text{Ca}$ -system provides a suitable test case. This particular choice is motivated by Ref. [17] where the applicability of TDHF was demonstrated up to very high energies. All calculations in this section were done for central collisions (impact parameter $b = 0$). The numerical grid was set up with 36×24^2 grid points.

A. Variation of the Skyrme force

In the first set of calculations we vary the Skyrme parametrization. Figure 1 shows the results of a central $^{40}\text{Ca}+^{40}\text{Ca}$ collision with the Skyrme parametrizations SLy4, SLy6 [18], SkMs [19], SkI3, and SkI4 [20]. While SkMs was chosen as an example for an outdated interaction, the SLy(X) set of forces was originally developed to study isotopic trends in neutron rich nuclei and neutron matter with applications in astrophysics. The SkI(X) forces take the freedom of an isovector spin-orbit force into account. This results in an improved description of isotopic shifts of r.m.s. radii in neutron-rich Pb isotopes.

The global development of the reaction is visualized in subplot (d). The time-dependent expectation value $Q_r^{20}(t)$ shows the five trajectories initially in good agreement but finally fanning out. A similar splitting behavior depending on the employed Skyrme parametrization was already found in [21]. While the two Sk(X)-forces show a full separation of the two fragments, there is a slight remaining contact between the fragments for the case of SLy6, which will result in complete separation in a longer calculation. However the trajectories for SLy4 and SkMs show a merged system in the final state, which was found to persist in long-time simulations.

We now consider the relationship between the observed characteristics in coordinate space with the dynamics in phase space. Subplot (a) shows the β_k -value, measuring the global deviation of the momentum distribution from a sphere. The initial β_k -peak is strongly damped for all five Skyrme-forces. While the time development for all parametrizations remain in phase up to the second peak, later it starts to vary and continue with damped

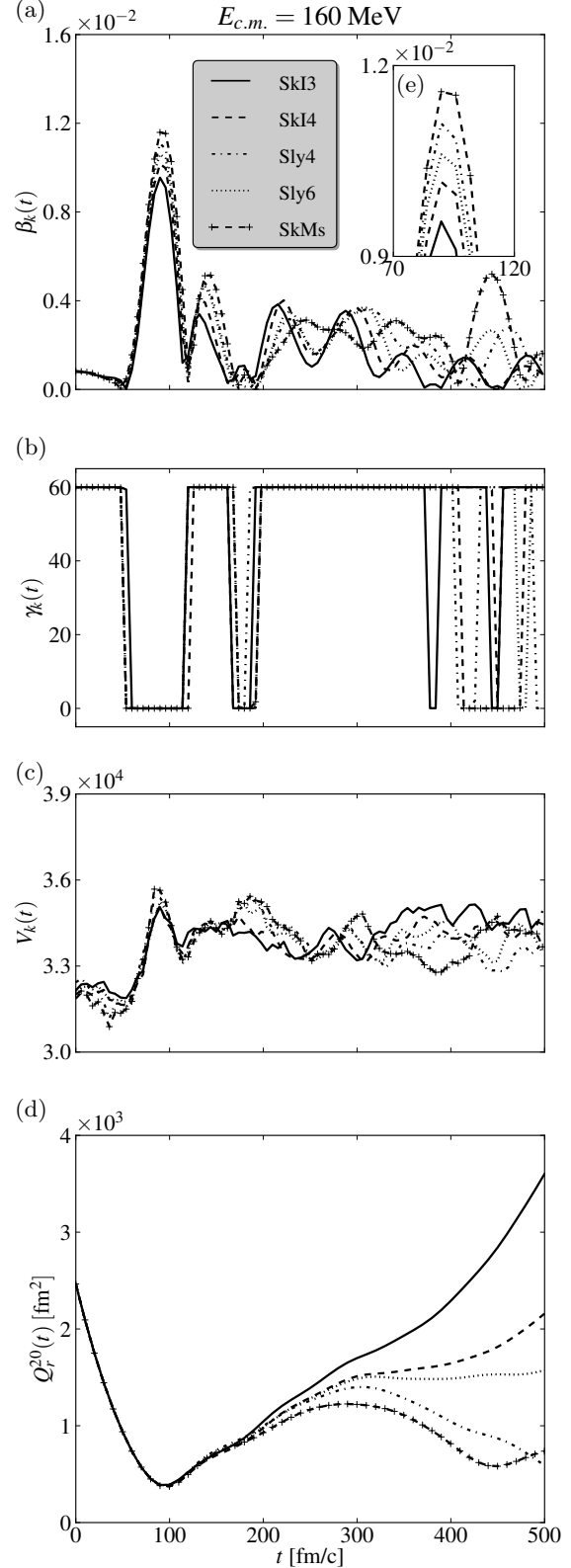


FIG. 1. Global observables $\beta_k(t)$ (a), $\gamma_k(t)$ (b), $V_k(t)$ (c), and $Q_r^{20}(t)$ (d) are shown for a central $^{40}\text{Ca}+^{40}\text{Ca}$ collision with a center-of-mass energy $E_{c.m.} = 160$ MeV. Each curve corresponds to a different Skyrme force as indicated in the legend.

TABLE I. Effective masses of Skyrme parametrizations used in this work are listed in connection with the maximal β_k -values from the plots (a, e) in Fig. 1.

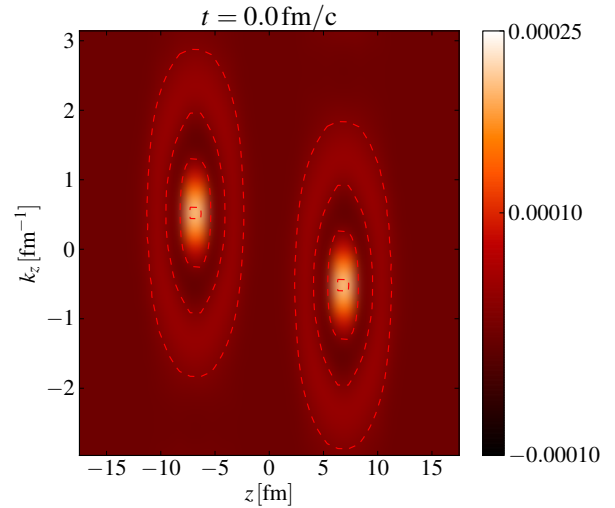
Skyrme force	m^*/m	β_k^{max}
SkM	0.79	0.0116
SLy4	0.70	0.0111
SLy6	0.69	0.0106
SkI4	0.65	0.0102
SkI3	0.57	0.0095

oscillations. For a better visualization the first peak is magnified in subplot (e). The taller the β_k -peak the longer the fragments will stick together in coordinate space. The effect appears to depend on the effective mass m^*/m . Smaller effective masses give rise to a smaller β_k -deformation. Table I summarizes the m^*/m -values associated with the maximal deformations β_k^{max} for all the Skyrme forces used in this work. It seems logical that the m^*/m -dependence is visible in the phase-space analysis since it is directly linked to the nucleons' kinetic motion. It is harder to randomize the directed motion of a nucleon with a higher effective mass than it is for a nucleon with a smaller m^*/m -dependence.

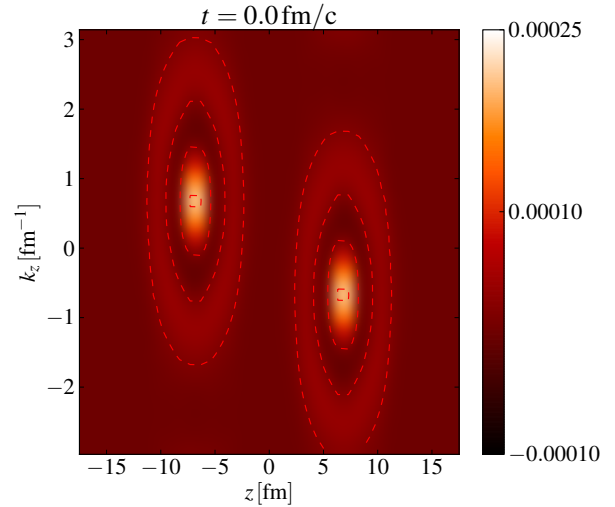
Subplot (b) shows the γ_k -value which indicates, whether a deformation is prolate, oblate, or triaxial [22]. For the present scenario of a central collision the γ_k -value jumps between prolate and oblate configurations indicating that the momentum distribution oscillates between being aligned primarily in the beam direction or transverse to it. For the sake of completeness we additionally present the occupied phase-space volume (c) which will prove more useful for the next reaction parameter to be discussed: the center-of-mass energy.

B. Variation with the center-of-mass energy

As a second reaction parameter the center-of-mass energy, $E_{c.m.}$, is varied. Results are presented for energies ranging from $E_{c.m.} = 2$ MeV/nucleon up to $E_{c.m.} = 3$ MeV/nucleon. The Skyrme interaction now is fixed to be SkI4. For the case of the lowest (highest) energy Video 1 (Video 2) provides a video visualizing the reaction in phase space. The calculation done with the lowest energy $E_{c.m.} = 160$ MeV shows two fully separated fragments in the exit channel. In contrast, the case with the highest energy (as well as the one at an intermediate energy) results in a merged system. The global observables are plotted in Fig. 2. It may not be obvious at first why the fragments should split for lower energies and merge for higher ones. But the estimate for the occupied phase-space volume $V_k(t)$ presented in subplot (c) indicates that V increases with energy. Therefore the fragments' average distance in phase space is larger, while in compensation they can come closer to each other in coordinate space. However, this behavior is also dependent



Video 1. (color online) Two-dimensional z - k_z -slice from the full six-dimensional Wigner distribution $f_W^{(3)}(\mathbf{r}, \mathbf{k})$ for a central $^{40}\text{Ca} + ^{40}\text{Ca}$ collision with a center-of-mass energy of $E_{c.m.} = 160$ MeV.



Video 2. (color online) Same as Video 2 with a center-of-mass energy of $E_{c.m.} = 240$ MeV.

on the particular Skyrme force used and the presence of time-odd terms, which is discussed in the next subsection.

C. Influence of time-odd terms

Skyrme energy-density functionals are calibrated to ground state properties of even-even nuclei [18–20]. This leaves the choice of the time-odd terms in the functional (current \mathbf{j}^2 , spin-density \mathbf{s}^2 , spin kinetic energy density \mathbf{T} , and the spin-current pseudotensor $\vec{\mathbf{J}}$) largely unspec-

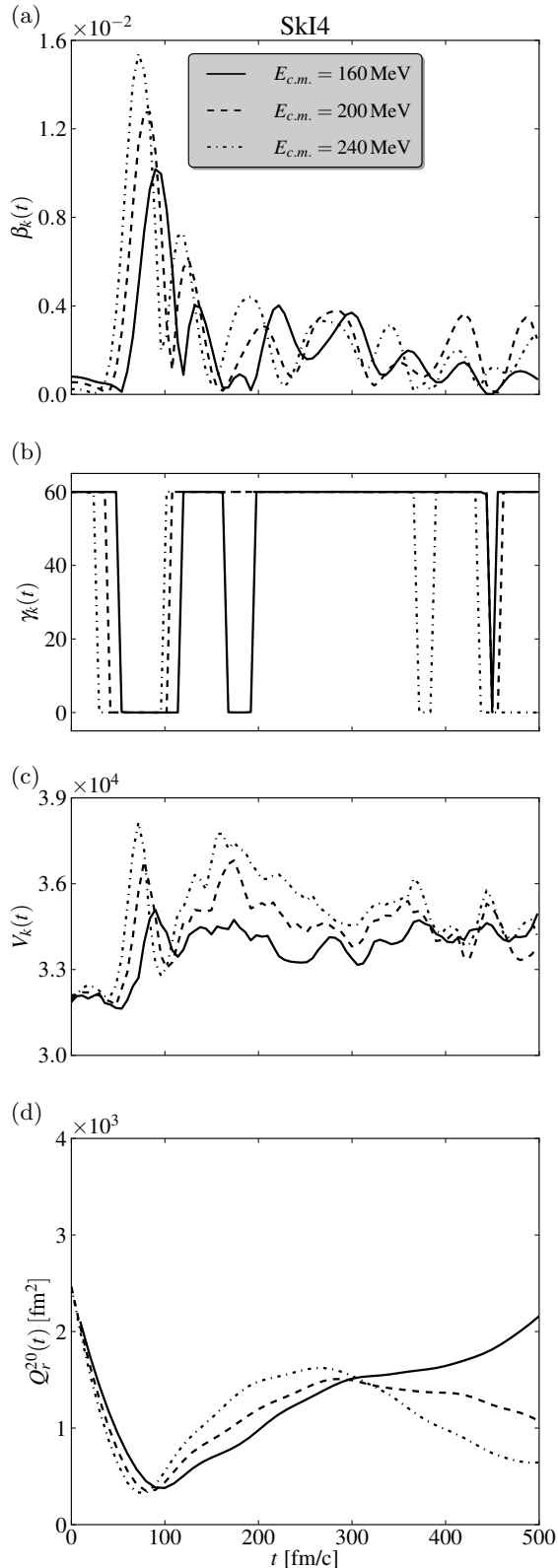


FIG. 2. Global observables $\beta_k(t)$ (a), $\gamma_k(t)$ (b), $V_k(t)$ (c), and $Q_r^{20}(t)$ (d) are shown for a central $^{40}\text{Ca}+^{40}\text{Ca}$ collision with fixed Skyrme interaction SkI4. Each curve corresponds to a different center-of-mass energy.

ified [24]. Galilean invariance requires at least some of these terms to be present depending on the presence of the associated time-even term, e.g. \mathbf{j}^2 for the $(\rho\tau - \mathbf{j}^2)$ combination. In our calculations we always include the time-odd part of the spin-orbit interaction. In order to investigate the effects of the remaining time-odd terms, we have compared different choices by using a single Skyrme parametrization and the same test case. We choose the force SLy4 and start with the minimum number of time-odd terms which is needed to ensure Galilean invariance [25]. In the next stage, we include also the spin-density terms proportional to \mathbf{s}^2 . Finally, we also add the combination which includes the tensor spin-current term $(\mathbf{s} \cdot \mathbf{T} - \vec{\mathbf{J}}^2)$. A comprehensive notation of the full Skyrme functional can be found, e.g. in Ref. [26]. As shown in Fig. 3, at least for the quantities β_k and Q_r^{20} , varying these time-odd terms has a very little effect in the initial contact phase and the dynamical behavior becomes somewhat different only in later stages of the collision. On the other hand, small differences near the threshold energy (the highest collision energy for a head-on collision that results in a composite system. At higher energies the nuclei go through each other) can have large long-term effects on the outcome of the collision. For example a small difference in dissipation may be enough to influence the decision between re-separation or forming a composite system. We have also checked a broader range of collision energies from the fusion regime up to deep inelastic collisions. The interesting quantity is the loss of fragment kinetic energy between the entrance and exit channels. It was found that the spin terms contribute small changes to this loss which can go in both directions, less dissipation near fusion threshold and more dissipation above. Subplot (b) of Fig. 3 shows the effects near the Coulomb barrier where spin terms reduce dissipation.

IV. SUMMARY

We have presented a geometrically unrestricted framework to study nuclear dynamics within TDHF in the full six-dimensional phase space. The impact of different reaction parameters on the outcome of a heavy-ion collision was studied in detail for the $^{40}\text{Ca}+^{40}\text{Ca}$ system. We find that the occurrence of transparency is clearly reflected in the global asymmetry of the Wigner momentum distribution. The surprising result that in some cases the system merges at higher energies and shows transparency at lower ones can be related to the interplay between momentum- and configuration-space volumes which is a reflection of the Pauli principle. It is also interesting that the two distributions in phase-space never truly combine to form a single distribution. This clearly indicates that two-body collisions will be necessary to achieve true equilibrium as the reaction proceeds to longer contact times. The detailed degree of relaxation found depends on energy and also the properties of the Skyrme force, where especially the effective mass seems to be impor-

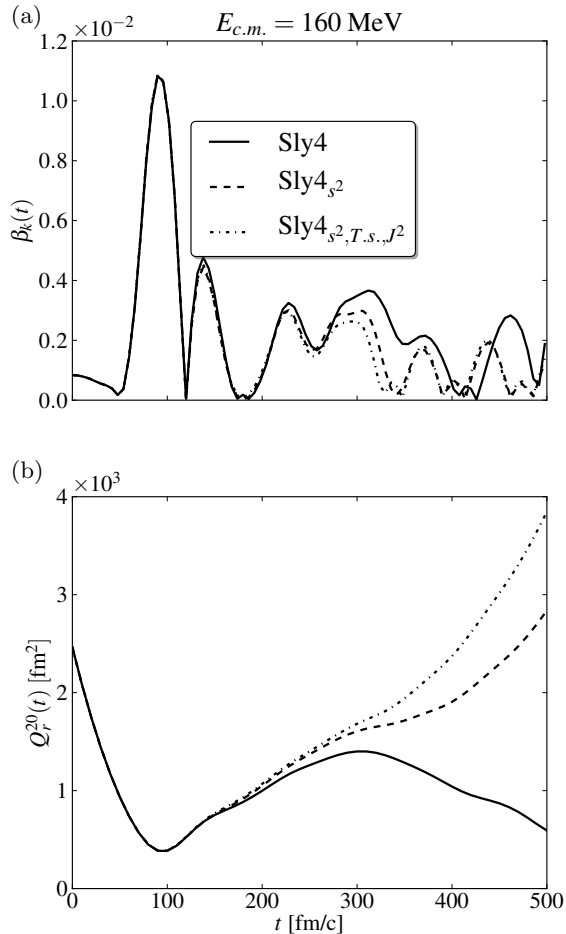


FIG. 3. Global observables $\beta_k(t)$ (a), and $Q_r^{20}(t)$ (d) are shown for a central $^{40}\text{Ca}+^{40}\text{Ca}$ collision with fixed Skyrme interaction SLy4.

tant. The presence of additional time-odd terms in the Skyrme functional appears to have a complex impact on the outcome of a collision as well. In this paper only one non-central collision was studied. A systematic investigation of impact parameter and energy dependence (fusion, deep-inelastic reactions) as well as even heavier systems would be highly interesting but is beyond computational feasibility at the moment.

ACKNOWLEDGMENT

This work has been supported by BMBF under contract Nos. 06FY9086 and 06ER142D, and the U.S. Department of Energy under grant No. DE-FG02-96ER40975 with Vanderbilt University. The videos linked in the manuscript can be found at <http://th.physik.uni-frankfurt.de/~loebl/vid1.mpeg> and <http://th.physik.uni-frankfurt.de/~loebl/vid2.mpeg>.

-
- [1] P. Bonche, S. E. Koonin, and J. W. Negele, Phys. Rev. C **13**, 1226 (1976).
 - [2] J. P. Svenne, Adv. Nucl. Phys. **11**, 179 (1979).
 - [3] J. W. Negele, Rev. Mod. Phys. **54**, 913 (1982).
 - [4] K. T. R. Davies, K. R. S. Devi, S. E. Koonin, and M. R. Strayer, in Treatise on Heavy-Ion Physics, Vol. 3 Compound System Phenomena, edited by D. A. Bromley (Plenum Press, New York, 1985), p. 3.
 - [5] K.-H. Kim, T. Otsuka, and P. Bonche, J. Phys. G **23**, 1267 (1997).
 - [6] C. Simenel and P. Chomaz, Phys. Rev. C **68**, 024302 (2003).
 - [7] T. Nakatsukasa and K. Yabana, Phys. Rev. C **71**, 024301 (2005).
 - [8] A. S. Umar and V. E. Oberacker, Phys. Rev. C **71**, 034314 (2005).
 - [9] J. A. Maruhn, P.-G. Reinhard, P. D. Stevenson, J. R. Stone, and M. R. Strayer, Phys. Rev. C **71**, 064328 (2005).
 - [10] Lu Guo, P.-G. Reinhard, and J. A. Maruhn, Phys. Rev. C, **77**, 041301 (2008).
 - [11] E. P. Wigner, Phys. Rev **40**, 749 (1932).
 - [12] N. Loebl, J. A. Maruhn, and P.-G. Reinhard, Phys. Rev. C **84**, (2011).
 - [13] J. A. Maruhn, Proc. Topical Conf. on Heavy-ion collisions, Oak Ridge National Laboratory report CONF-770602, Fall Creek Falls State Park, TN (1977).
 - [14] V. Blum, G. Lauritsch, J. A. Maruhn, and P.-G. Reinhard, J. Comput. Phys. **100**, 364 (1992).
 - [15] P.-G. Reinhard and R. Y. Cusson, Nucl. Phys. **A378**, 418 (1982).
 - [16] H. Flocard, S. E. Koonin, and M. S. Weiss, Phys. Rev. **C17** (1978) 1682-1699.
 - [17] C. Simenel, Phys. Rev. Lett. **106**, 112502, (2011).
 - [18] E. Chabanat, E. P. Bonche, P. Haensel, J. Meyer, and R. Schaeffer, Nucl. Phys. A **635**, 231 (1998).
 - [19] J. Bartel, P. Quentin, M. Brack, C. Guet, and H.-B. Håkansson, Nucl. Phys. **A386**, 79 (1982).
 - [20] P.-G. Reinhard and H. Flocard, Nucl. Phys. A **584**, 467 (1995).
 - [21] J. A. Maruhn, K. T. R. Davies, M. R. Strayer, Phys. Rev. **C31**, 1289-1296 (1985).

- [22] W. Greiner, and J.A. Maruhn, “Nuclear models”, Springer-Verlag, Berlin, New York (1996).
- [23] S. Heinz, V. Comas, F. P. Heßberger, S. Hofmann, D. Ackermann, H. G. Burkhard, Z. Gan, J. Heredia, J. Khuyagbaatar and B. Kindler, *et al.*, *The European Physical Journal A - Hadrons and Nuclei*, Springer Berlin / Heidelberg, 2008, **38**, 227-232.
- [24] M. Bender, P.-H. Heenen, and P.-G. Reinhard, *Rev. Mod. Phys.* **75**, 121 (2003).
- [25] Y. M. Engel, D. M. Brink, K. Goeke, S. J. Krieger, and D. Vautherin, *Nucl. Phys. A* **249**, 215 (1975).
- [26] T. Lesinski, M. Bender, K. Bennaceur, T. Duguet, and J. Meyer, *Phys. Rev.* **C76**, 014312 (2007).